

The effects of stellar populations on galaxy scaling relations in the 6dF Galaxy Survey

Robert N. Proctor¹, Philip Lah², Duncan A. Forbes¹, Matthew Colless³
and Warrick Couch¹

¹ Centre for Astrophysics & Supercomputing, Swinburne University, Hawthorn VIC 3122, Australia

Email: rproctor@astro.swin.edu.au, dforbes@astro.swin.edu.au, wcouch@astro.swin.edu.au

² Research School of Astronomy & Astrophysics, Australian National University, Weston Creek, ACT 2611, Australia

Email: plah@mso.anu.edu.au

³ Anglo-Australian Observatory, PO Box 296, Epping, NSW 1710, Australia

Email: colless@aao.gov.au

3 November 2018

ABSTRACT

We present an analysis of the stellar populations as a function of mass in a sample of ~ 7000 galaxies of all morphological and emission types from the 6dF Galaxy Survey (6dFGS). We measure velocity dispersions and Lick indices from the spectra of the central regions of these galaxies, deriving ages and metallicities from the Lick indices using stellar population models. We also derive dynamical masses and dynamical mass-to-light ratios for these galaxies by combining the central velocity dispersions with global photometry in the B, R and K bands from SuperCOSMOS and 2MASS. Together, these data allow us to reduce the degeneracies between age, metallicity and star formation burst-strength that have limited previous studies.

We find that old galaxies exhibit a mass-metallicity relation with logarithmic slope $d[\text{Fe}/\text{H}]/d\log M \approx 0.25$, while young galaxies show slopes consistent with zero. When we account for the effects of the mass-metallicity relation, we obtain a single, consistent relation between mass-to-light ratio and mass for old galaxies in all passbands, $M/L \propto M^{0.15}$. As we have accounted for stellar population effects, this remaining variation in the mass-to-light with mass (the residual ‘tilt’ of the Fundamental Plane) must have a dynamical origin. However, we demonstrate that any simple trend between mass-to-light-ratio and mass or luminosity is inconsistent with the observations, and that a more complex relationship must exist.

We find that the central regions of galaxies of all masses often exhibit young stellar populations. However it is only in the lowest-mass galaxies studied ($\sim 10^{10} M_{\odot}$) that these populations are evident in the global photometry. In higher-mass galaxies, young central populations have decreasing influence on the global photometry, with there being no discernible impact in galaxies more massive than $\sim 2 \times 10^{11} M_{\odot}$. We conclude that the young stellar populations detected in spectroscopic studies are generally centrally concentrated, and that there is an upper limit on the mass of star-forming events in massive galaxies. These results have important ramifications for mass-to-light ratios estimated from photometric observations.

Key words: galaxies: general, galaxies: stellar content, galaxies: kinematics and dynamics

1 INTRODUCTION

Current models of galaxy formation and assembly can be characterised by two extreme and competing views. One such view is represented by the early “monolithic collapse” model, whereby the spheroidal (bulge) components of galax-

ies form by the early collapse of individual gas clouds (e.g. Larson 1974; Carlberg 1984). In these early collapse models the star formation induced by the collapse is terminated when the source of gas is either consumed or expelled from the galaxy. The bulge then ages passively (albeit perhaps subject to the later addition of a disk). Such models are

largely motivated by the small scatter in the observed relationships between colour and magnitude (e.g. Baum 1959; Bower, Lucy & Ellis 1992a,b) and velocity dispersion, surface brightness and size (the Fundamental Plane; Dressler et al. 1987) for early-type galaxies and bulges. To explain the tightness of these relations, early collapse models require that star formation in bulges terminates at early times ($z \geq 2$; Bower, Lucy & Ellis 1992a,b), so that bulge dominated (e.g. elliptical) galaxies should be uniformly old.

This picture faces challenges on a number of fronts. For instance, the differing slopes found for the Fundamental Plane in various bands (e.g. Bernardi et al. 2003b) are difficult to explain in the monolithic collapse scenario. Furthermore, spectroscopic studies of the stellar populations in the bulges of galaxies find central ages ranging from ~ 1 –15 Gyr (e.g. Trager et al. 2000; Proctor & Sansom 2002; Terlevich & Forbes 2002; Caldwell, Rose & Concannon 2003; Kauffmann et al. 2003a,b; Proctor et al. 2004b), indicating evidence for more recent star formation.

However, by far the most important challenge to the early collapse picture is the fundamental differences in galaxy formation and assembly histories that are predicted when the growth of structure via gravitational instability is modelled for a dark matter-dominated universe, now characterised extremely well via precision measurements of the cosmological parameters (e.g. the Λ CDM model; Spergel et al. 2003). Such ‘‘hierarchical’’ models, which represent the other extreme view, predict galaxy-mass objects to be assembled by the successive merging of lower-mass objects via hierarchical merging (White & Rees 1978), usually over an extended period.

Another important prediction of hierarchical merging models is that the merger rate of galaxies is a function of environment, i.e. on average, galaxies in the dense environs of clusters merge early, while those in the less dense ‘field’ merge later (Kauffmann 1996). In the hierarchical merging scenario the properties of galaxies are therefore subject to strong influences from their environment. Results from stellar population studies appear to confirm the prediction of hierarchical merging models in that ‘field’ galaxies possess slightly younger central ages than their cluster counterparts (e.g. Thomas et al., 2005; Bernardi et al., 2006; Smith et al., 2006).

In contrast to early collapse models, hierarchical merging models predict galaxy bulges to possess a range of ages, with low-mass galaxies forming earlier, and on shorter timescales, than high-mass galaxies. At first glance, the wide range of ages observed in spectroscopic studies might also appear to confirm the hierarchical merging predictions, however the observed trend of age with mass is for lower-mass systems to be *younger* than higher-mass systems. This is inconsistent with hierarchical merging models which predict lower-mass systems to form earlier than high-mass system (Kauffmann 1996). The observed trend is therefore sometimes referred to as ‘anti-hierarchical’.

The recent De Lucia et al. (2006) analysis of the Millennium Simulation provides insights important to the development of a coherent picture of galaxy evolution. The Millennium Simulation models the evolution of dark matter using an N-body code to which De Lucia et al. couple a semi-analytic model of galaxy formation. De Lucia et al.’s analysis clearly demonstrates that a strong distinction must

be made between the *mass assembly* of galaxies and the *formation* of their stellar populations. This can be understood intuitively by the simple realisation that mergers bring old stars into a merger remnant as well as making new stars. Merger remnants may therefore be, and often are, still dominated (in terms of their mass) by old stellar populations. De Lucia et al. conclude that while the mass assembly of galaxies is indeed hierarchical, their star formation histories are nevertheless anti-hierarchical. Despite this improvement in our theoretical understanding, the problem remains how to reconcile the broad range of predicted (and spectroscopically observed) galaxy ages with the extremely small scatter in some scaling relations.

Recent surveys of large numbers of nearby galaxies have provided statistically significant results and hence further observational constraints on galaxy formation models. Such surveys include the 2dF Galaxy Redshift Survey (2dFGRS; Colless et al. 2001b) and the Sloan Digital Sky Survey (SDSS; York et al. 2000). From central region spectra and global optical colours the 2dFGRS probed the cosmic star formation history at relatively low redshift (Baldry et al. 2002) and its variation with local environmental density (Lewis et al. 2002). The SDSS also obtained optical colours and central spectra for a large number of low redshift galaxies. This ongoing dataset has been used by several authors to study the star formation history and scaling relations of nearby galaxies. These studies include Bernardi et al. (2003b) who investigated scaling relations for $\sim 9,000$ galaxies, Eisenstein et al. (2003) who combined spectra of 22,000 massive galaxies, Gallazzi et al. (2005) who probed the star formation history of $\sim 40,000$ galaxies, Cid Fernandes et al. (2005) who conducted a spectral synthesis of $\sim 50,000$ galaxies, and Chang et al. (2006) who combined spectra and optical colours with 2MASS near-infrared colours for $\sim 3,000$ galaxies. Such large datasets have allowed these authors to investigate trends as a function of mass, environment, galaxy type etc. Already, a galaxy mass-metallicity relation has been detected in the metallicities of both gas (Tremonti et al. 2004) and stars (Gallazzi et al. 2005) and strong trends with galaxy environment identified (Lewis et al. 2002).

However, the above studies have not explicitly explored the link between the *central* stellar populations, which they observe, and the *global* photometry of the galaxies in their samples. It is this issue that this paper specifically addresses. To this end, we compare the results of stellar population analysis of spectra from the 6dF Galaxy Survey (6dFGS; Jones et al. 2004) to the global near-infrared photometry of the 2MASS Extended Source Catalog (2MASS XSC; Jarrett et al. 2000a,b) and optical SuperCOSMOS (Hambly, Irwin & MacGillivray. 2001) data for several thousand galaxies. We explore such issues as the fraction of galaxies’ stellar populations that can have been formed in recent star formation events and the effects of stellar populations on the slopes of colour-magnitude relations and the varying ‘tilt’ of the Fundamental Plane.

The paper is laid out as follows. In the next section we outline the photometric and spectroscopic data. In Section 3 we detail the spectroscopic data reductions and analysis used to derive stellar population parameters. Section 4 presents the results of our analysis, which are discussed and summarised in Section 5.

2 THE SAMPLE DATA

2.1 The 6dF Galaxy Survey

The 6dFGS is a spectroscopic survey of the entire southern sky more than 10 degrees from the Galactic Plane. The survey measured redshifts for more than 124,000 galaxies. The primary survey targets were selected primarily from the 2MASS Extended Source Catalog (XSC). All galaxies brighter than $K_{tot}=12.75$ were included in the sample. Secondary samples of 2MASS and SuperCOSMOS galaxies, complete down to magnitude limits $(H, J, r_F, b_J) = (13.00, 13.75, 15.60, 16.75)$, were also included.

The survey was carried out on the UK Schmidt Telescope using the Six-Degree Field (6dF) multi-fibre spectrograph. The 6dF instrument simultaneously observed up to 150 spectra over a 5.7° field. The science fibres of the instrument were 6.7 arcsec in diameter. The spectrograph is bench mounted in an enclosure inside the telescope dome, which gives it increased instrumental stability compared to a spectrographs mounted on a telescope (e.g. 2dF and the SDSS spectrograph). This increased instrumental stability maintains consistent instrumental resolution, which is important when working with Lick indices. The survey obtained spectra in the visual (V) and red (R) wavelength ranges providing coverage from ~ 4000 to $\sim 8400\text{\AA}$. The spectra have 5-6 \AA FWHM resolution in V and 9-12 \AA resolution in R (see Jones et al. 2004 for more details).

The main science aims of the survey included: to measure the luminosity function of near-infrared selected galaxies as a function of environment and galaxy type (Jones et al. 2006), to measure the clustering of galaxies, to produce detailed maps of the density and peculiar velocity fields of the nearby universe (Jones et al. 2004; Erdogdu et al. 2006) and to study the properties of the underlying stellar population of the galaxies such as ages and chemical abundances. It is this latter issue to which this paper is addressed.

The 6dFGS is particularly suited to the aims of the current study because the selection criteria using 2MASS near-infrared photometry provides a sample less biased toward bright, young galaxies than surveys based on optical catalogues. The K band photometry also has the useful property of being relatively insensitive to both metallicity the presence of dust (unlike optical bands), and is therefore an good tracer of mass. It also provides a useful tool in breaking the age-metallicity degeneracy. Finally, 6dFGS spectra are obtained from region 2 to 3 times larger on the sky than those used in the 2dFGRS and SDSS surveys. As a result, at the mean redshifts of the surveys, 2dF, SDSS and 6dFGS fibres correspond to 2.6, 3.9 and 4.6 kpc/h respectively. The 6dFGS spectra therefore sample a significantly larger fraction of the total galaxy light than either 2dF or SDSS spectra.

2.2 Spectroscopic data

The spectroscopic data presented here are from the 6dFGS First Data Release (Jones et al. 2004). Lick index, velocity dispersion and emission line-strength measurements were made on all galaxies with redshift quality ≥ 3 (the ‘reliable’ redshifts; Jones et al. 2004). This gave a

total of 39649 galaxies with 3859 of these observed more than once (420 galaxies observed more than twice). If a galaxy was observed more than once, only the highest signal-to-noise-ratio spectrum was used for the measurements. However, repeat observations were used to establish the errors (see Section 3.5). Only galaxies with median signal-to-noise ratios $\geq 12 \text{\AA}^{-1}$ were deemed suitable for age and metallicity determinations. Such a value lies at the lower limit of signal-to-noise-ratio that can be used to derive ages and metallicities with precision. The above selection criteria resulted in ~ 7000 galaxies suitable for Lick index measurements. It should be noted that, as no morphological selection was made, the results presented here include galaxies of the full range of early and late types.

2.3 Photometric data

The K band magnitudes used in this work were taken to be the K_{tot} values estimated from the 2MASS data by Jones et al. (2004). We also use the re-calibrated SuperCOSMOS B and R band magnitudes (Hambly et al. 2001). Galaxy radii were taken as the 2MASS 20th magnitude per arcsec² isophotal radius (R_{K20} ; Jarrett et al. 2001a). We also use K band half-light (effective) radii (R_{eff}) for a spectroscopically selected early-type galaxy subsample, as supplied by Lachlan Campbell (private communication). Absolute magnitudes and physical galaxy radii were calculated using distances based on the measured redshifts and a Hubble constant of $70 \text{ km s}^{-1} \text{ Mpc}^{-1}$ (our median redshift is 0.035). Errors on the distance estimates were assumed to be a combination of recession velocity uncertainty and peculiar motions. In order to be conservative, we assumed the combined uncertainty to be $\pm 1000 \text{ km s}^{-1}$. The distributions of some key parameters in the final sample are shown in Fig. 1. The sample covers of order 5 magnitudes in luminosity ($-26 \leq M_K \leq -21 \text{ mag}$ and $-22 \leq M_B \leq -17 \text{ mag}$). This corresponds to a dynamical mass range of more than two orders of magnitude (from $< 10^{10}$ to $> 10^{12} M_\odot$; Section 4.4). From the sample of ~ 7000 galaxies suitable for age-metallicity determination (Section 2.2) ~ 6000 also had a full set of 2MASS and SuperCOSMOS photometry.

3 SPECTROSCOPIC ANALYSIS

3.1 Measuring emission lines

We measured emission line-strengths for $H\alpha$, $H\beta$, $[\text{NII}]\lambda 6548$, $[\text{NII}]\lambda 6584$, $[\text{OIII}]\lambda 4959$ and $[\text{OIII}]\lambda 5007$ from the 6dFGS spectra. In order to measure the $H\alpha$ and $[\text{NII}]$ emission, a de-blending option in the IRAF task *split* was used. This option allows the fitting of Gaussians to a series of spectral lines and the measurement of the value of the equivalent widths of each. The strengths of $H\alpha$ and the two $[\text{NII}]$ doublet lines either side of it were measured in this way from continuum divided spectra. This process can lead to false measurements where noise spikes or the continuum level are fit with Gaussian profiles rather than real features. By consideration of the position and FWHM of the Gaussian fit to the feature, one can reasonably discriminate between real emission features and

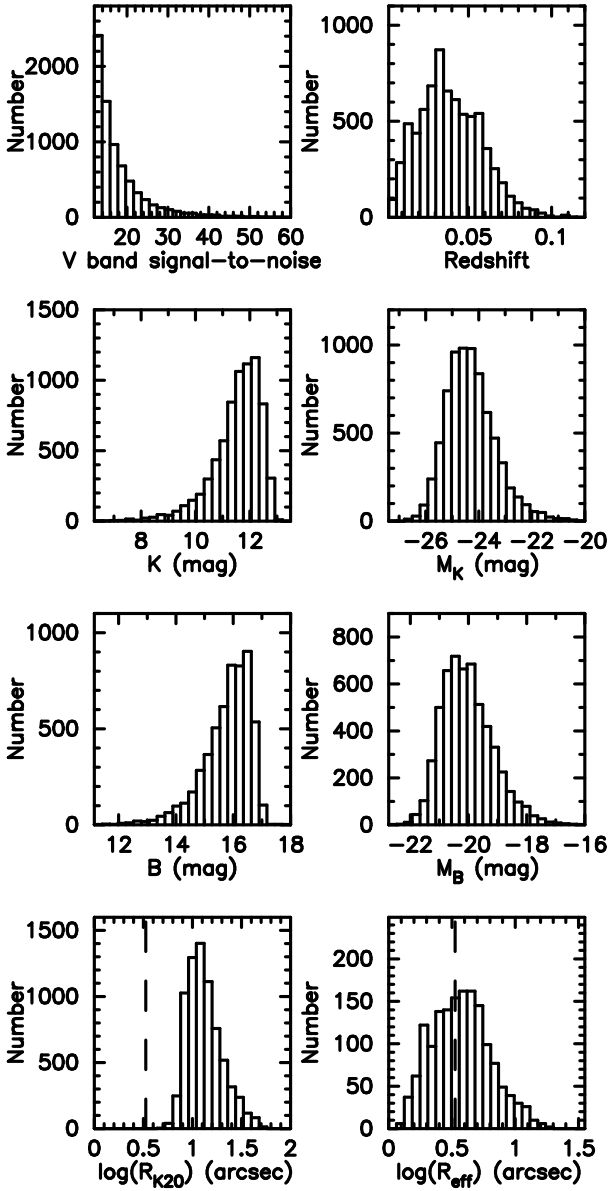


Figure 1. The distributions of key parameters in the final sample of ~ 7000 galaxies presented here. The signal-to-noise-ratio per \AA is estimated as the median of the 6dFGS spectra. Apparent magnitudes are from 2MASS and SuperCOSMOS data. Absolute magnitudes were calculated using redshifts from the 6dFGS spectra and a Hubble constant of $70 \text{ km s}^{-1} \text{ Mpc}^{-1}$. K band 20th magnitude isophotal radius is from 2MASS. Effective radii are also presented for a ($\sim 25\%$) subsample of our 6dFGS galaxies. Dashed lines in the radius plots represent the radius of the 6dF aperture (3.35 arcsec).

false detections. If the line centre was more than 7 \AA away from the features expected wavelength (given the 6dFGS redshift), the measurement was discarded. If the FWHM was well below the instrumental resolution of the 6dF instrument ($< 5 \text{ \AA}$) the measurement was also discarded. Finally, extremely large FWHM ($> 12 \text{ \AA}$) were discarded. These large FWHM are mostly Gaussian fits to features in the continuum, but may also have occasionally included real features of broad-lined active galactic nuclei (AGN).

The equivalent widths of the two [OIII] emission lines

at 4959 and 5007 \AA were measured using the procedure and band definitions of Gonzalez (1993). $H\beta$ emission, on the other hand, was estimated for each galaxy as the difference between the *observed* 6dFGS $H\beta$ index value and the value predicted by our best-fit model solutions (see Section 3.6).

Within this work the sample is sometimes subdivided into ‘passive’ (no emission) and ‘emission’ galaxies. Passive galaxies are defined as those in which no emission lines are detected within the 6dFGS wavelength range with greater than approximately $1\text{-}\sigma$ significance. Emission line galaxies are therefore defined as those in which at least one emission line is detected at greater than one sigma confidence. For $H\alpha$ this criterion corresponds to emission-line equivalent widths of $\sim 1.5 \text{ \AA}$. Using this definition the sample contains 4640 passive galaxies and 2270 emission galaxies. Unfortunately, a full analysis of morphological types is not available for the sample. However, visual inspection of a sub-sample of passive galaxies suggests that $\sim 80\%$ are early types, while amongst the emission galaxies a similar fraction are late types.

3.2 Measuring velocity dispersion

The method used to measure Lick indices from appropriately broadened spectra and to correct the indices for the broadening effect of a galaxy’s velocity dispersion was based on that used by Stephen Moore (2001)

Measurements of the velocity dispersion in the 6dFGS galaxy spectra were made using the IRAF task *fxcor* which carries out a Fourier cross-correlation between the object spectrum and a zero-redshift, zero-velocity dispersion template spectrum. The task outputs the radial velocity of the object spectrum and the FWHM of the Fourier correlation peak between the object and template spectra, which can be converted into a velocity dispersion. The template spectra used were three velocity standard stars observed with the 6dF spectrograph in 2003 March by Craig Harrison (HR2574, HR3145 and HR5888, which are late G and early K giants).

The raw values of the velocity dispersion measured by *fxcor* need to be calibrated. To do this each of the standard star spectra were artificially broadened to a specific velocity dispersion using the IRAF task *gauss*. These artificially broadened spectra were then used to calibrate their (known) velocity dispersions against the value measured by *fxcor*. Towards lower velocity dispersions, as one approaches the instrumental velocity resolution ($\lesssim 100 \text{ km s}^{-1}$), this calibration becomes less accurate. However, galaxies with such low velocity dispersions require only very small corrections to their measured Lick index values. Consequently, reliable index determinations can still be obtained in low velocity dispersion galaxies. More importantly, this method of measuring velocity dispersion fails on galaxies that are not well fit by the standard star templates. This mainly occurs in low signal-to-noise ratio galaxy spectra with young ages and/or strong emission lines.

A comparison of velocity dispersion values derived from the 6dFGS spectra to values in the literature (Hyperleda) is shown in Fig. 2. The 6dFGS values show good agreement with the literature values with an average offset of -6.1 km s^{-1} , and an RMS scatter of 20 km s^{-1} . Both deviation and scatter are greatest at high velocity dispersion, where

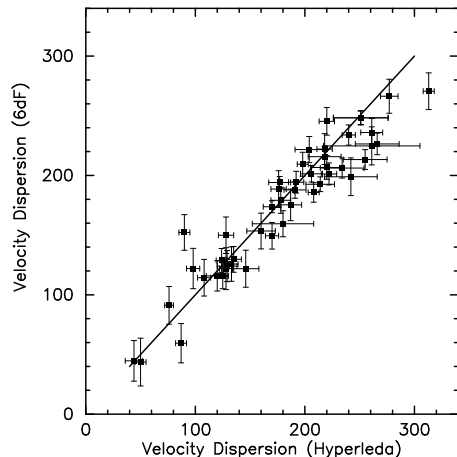


Figure 2. A comparison of velocity dispersion derived from 6dFGS spectra (in km s^{-1}) with values from the literature (Hyperleda). Despite the large 6dF aperture we find an offset from the one-to-one line (shown as a solid line) of only 6 km s^{-1} with an RMS scatter of 20 km s^{-1} . Such differences have only small effects on Lick index determinations.

we find the Hyperlead values to be consistently greater than the 6dFGS values. This is in agreement with Bernardi (2007) who found Hyperleda values greater than values derived from the SDSS at high velocity dispersion.

Given the large 6dF aperture (6.7 arcsec compared to a more typical 2 or 3 arcsec in Hyperleda) it is possible that these deviations are the results of aperture effects. Jørgensen et al. (1995) investigated the effects of varying the aperture size in observations of velocity dispersions in the inner regions (i.e. $R \lesssim R_{\text{eff}/2}$) of early-type galaxies. Their results showed a weak power law dependence of measured velocity dispersions with the size of aperture. We therefore experimented with correcting velocity dispersions according to Jørgensen et al. (1995) in the sub-sample of 6dFGS galaxies for which Hyperlead values were also available. As this sub-sample of the data is heavily biased to nearby, early-type galaxies, it is well matched to the galaxies used to calibrate the Jørgensen et al. (1995) relation. The results showed that while the offset was reduced to $+0.75 \text{ km s}^{-1}$, the scatter was increased to 23 km s^{-1} . We also note that the trend for Hyperleda values to be greater than values derived from our data remains unaffected by these corrections.

As noted above, the Jørgensen et al. (1995) correction is calibrated for the inner regions of early-type galaxies. However, for our 6dFGS sample as a whole, the *average* aperture is $\sim 1 R_{\text{eff}}$ (see Fig. 1). The sample also contains both early- and late-type galaxies. This suggests that the corrections presented by Jørgensen et al. (1995) are inappropriate for the 6dF sample as a whole. For such a sample, it is instead informative to consider the study of Gebhardt et al. (2000). This analysis of the variation in observed velocity dispersions (including the effects of rotation) measured through circular apertures of varying radius in a sample of 26 galaxies of mixed Hubble types shows that, within $5 R_{\text{eff}}$, the sample exhibits little or no systematic variation of the measured velocity dispersion with aperture size.

As a result of the considerations above, we have elected to make no corrections for aperture size to the measured

velocity dispersion values within this work.

3.3 Measuring Lick indices

To make Lick index measurements suitable for direct comparison with single stellar population (SSP) models, it is necessary to broaden the spectra to the instrumental resolution of the Lick/IDS system. The Lick/IDS FWHM instrumental resolution as a function of wavelength is described in Worthey & Ottaviani (1997) where it is shown to vary from $\sim 8.5 \text{ \AA}$ at the central wavelength ($\sim 5000 \text{ \AA}$) to $\sim 10 \text{ \AA}$ at the spectrum ends (~ 4000 and 6000 \AA).

The calculation of the necessary broadening requires the measurement of the 6dF instrumental resolution. This was measured from 6dF arc line spectra obtained from the observational time-span of the 6dFGS First Data Release. The instrumental resolution of the 6dF spectra varies not only with wavelength but also with optical fibre number, so measurements were made of arc lines at various wavelengths, *for all fibres individually*. A bivariate polynomial was fit to the measured FWHM spectral resolution as a function of both wavelength and fibre number. The amount of broadening required to match the Lick/IDS resolution could then be estimated and each 6dF spectrum was broadened to this resolution.

3.4 Velocity dispersion correction

The index values given in stellar population models do not include the effect of the velocity dispersion broadening present in galaxy spectra. It is therefore necessary to introduce a correction to the observed galaxy index values to account for this effect.

To measure the velocity dispersion correction required for each Lick index, we measured the indices of a range of artificially broadened stellar spectra. These values of the Lick indices measured in the broadened spectra were then compared to those measured in the un-broadened spectra to determine the index corrections for a range of velocity dispersions.

For each index measured in Angstroms (e.g. the Fe and Ca indices) a multiplicative correction was defined by:

$$\text{Index correction} = \frac{\text{Index}_{\sigma=0}}{\text{Index}_{\sigma}} \quad (1)$$

While, for each index measured in magnitudes (e.g. CN_1 , CN_2 , Mg_1 , Mg_2), an additive correction was defined by:

$$\text{Index correction} = \text{Index}_{\sigma=0} - \text{Index}_{\sigma} \quad (2)$$

Where $\text{index}_{\sigma=0}$ is the value of the index in the raw stellar spectrum (i.e. with no broadening) and index_{σ} is the index value after broadening of the stellar spectrum to a specific velocity dispersion σ .

For each index, quadratic lines were fitted to the velocity dispersion versus index correction ratio data. The index correction required for a particular galaxy could then be determined from the measured velocity dispersion and the quadratic function.

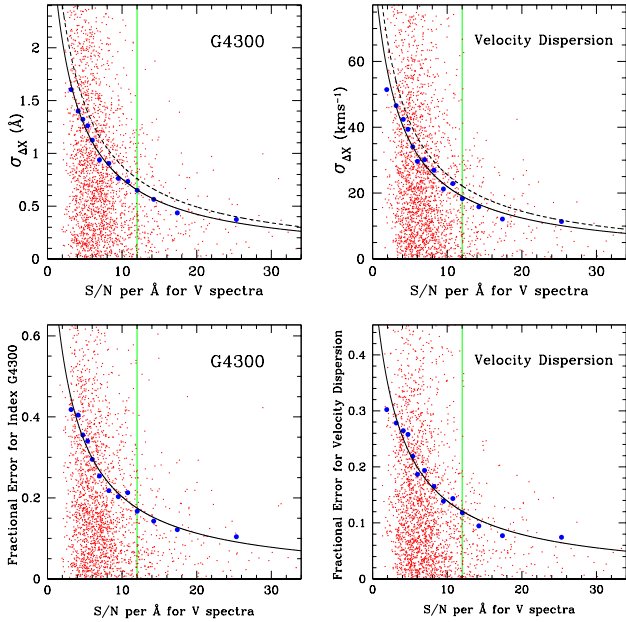


Figure 3. Top: The measured relationship between RMS error and signal-to-noise ratio from repeated observations for the G4300 index (left hand plot) and for velocity dispersion (right plot). The small points are the individual differences between repeated observations for each galaxy. The large points are the RMS binned values of these points after 2σ clipping. The solid line is the least squares fit to the bin values. The dashed line is the relationship between error and signal-to-noise ratio after correcting for the clipping used in forming the RMS bins (see Section 3.5). The vertical line marks the lowest signal-to-noise ratio (12 \AA^{-1}) used in the present study. **Bottom:** Same as top plots except the *fractional* error is shown.

3.5 Estimating errors

Estimating errors for spectroscopic measurements is notoriously difficult, mainly because there are several sources of error that can not be well quantified (e.g. sky-subtraction, poor flux calibration etc). Therefore, instead of trying to propagate variance arrays, comparisons of the values from repeated 6dFGS observations of the same galaxy were used to quantify this error. This method was used for calculating the error in Lick indices and velocity dispersions, as well as in $H\alpha$ and [NII] emission equivalent-widths.

In the First Data Release of the 6dFGS, 3859 galaxies were observed more than once. For all repeat observations the differences in values were grouped into bins based on the median signal-to-noise ratio of the galaxy spectra. The signal-to-noise ratio of the lower of the two observations was used for this binning, as this observation would be the cause of most of the error. If a galaxy had been observed more than twice then the two highest signal-to-noise ratio spectra were used. The RMS of each signal-to-noise ratio bin was determined and used as the $\sigma_{\Delta x}$ value. To remove the biasing effect of large outliers in the bins only the lowest 95.45% of the values (the 2σ limit) in each bin was used to calculate the RMS value. This requires that the RMS be scaled up by 1.164 to take into account this clipping.

A function was fitted to the RMS of the bins against the signal-to-noise ratio. The fitting function used was a modi-

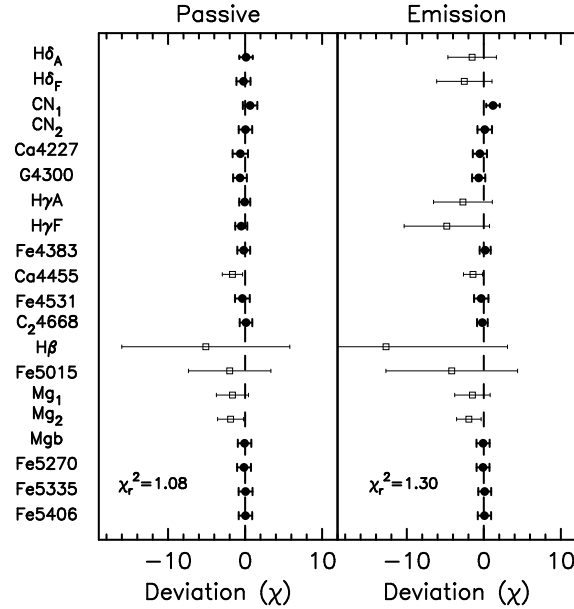


Figure 4. Mean residuals of indices to the final best-fit SSP models are given in units of observational error (i.e. χ). Error bars represent the RMS scatter about the mean. Solid symbols represent indices included in the fits, while open symbols represent those indices excluded from the fits. The results for fits to both passive (left) and emission galaxies (right) are shown. The average *reduced*- χ^2 of indices included in each subsample (χ_r^2) is indicated in each plot.

fied rectangular hyperbola of the form $y = a/(x+b)$ (a and b the fitted coefficients). The error in any measured quantity for a galaxy could then be estimated using the signal-to-noise ratio of the spectrum and the corresponding error from the fitted function. Examples of this procedure can be seen in Figure 3. We note that the majority of the sample with repeat measurements were re-sampled due to the low signal-to-noise of the original observation.

3.6 Fitting indices to models

We used the χ^2 -fitting procedure of Proctor & Sansom (2002) (see also Proctor et al. 2004a,b and Proctor et al. 2005) to measure the derived parameters: $\log(\text{age})$, $[\text{Fe}/\text{H}]$, $[\text{Z}/\text{H}]$ and $[\text{E}/\text{Fe}]$ (a proxy for the α -abundance ratio; see Thomas et al. 2003 for details). Briefly, the technique for deriving these parameters involves the simultaneous comparison of as many observed indices as possible to models of single stellar populations (SSPs). The best fit is found by minimising the square of the deviations between observations and models in terms of the observational errors (i.e. χ^2). The rationale behind this approach is that, while all indices show some degeneracy with respect to each of the derived parameters, each index does contain *some* information regarding each parameter. In addition, such an approach should be relatively robust with respect to many problems that are commonly experienced in the measurement of spectral indices and their errors. These include poor flux calibration, poor sky subtraction, poorly constrained velocity dispersions, poor calibration to the Lick system and emission-line contamination. This robustness is of particular importance in the analysis of large numbers of pipe-line reduced

spectra such as those of the 6dFGS which cannot be flux calibrated and so are not fully calibrated to the Lick system. The method is also relatively robust with respect to the uncertainties in the SSP models used in the interpretation of the measured indices; e.g. the second parameter effect in horizontal branch morphologies and the uncertainties associated with the Asymptotic Giant Branch. It was shown in Proctor et al. (2004a) and Proctor et al. (2005) that the results derived using the χ^2 technique are, indeed, significantly more reliable than those based on only a few indices.

In order to carry out the comparison of observations to SSP models it was first necessary to select and interpolate the models provided in the literature. Interpolations are required because models in the literature are presented at only five or six discrete metallicities over the ~ 2.5 dex range. We experimented with a number of different models (Bruzual & Charlot 2003 (hereafter BC03); Thomas, Maraston & Bender 2003; Thomas, Maraston & Korn 2004 and Korn, Maraston & Thomas 2005 (hereafter KMT05). The results presented here are those from the models of KMT05, as these provide the necessary coverage in age (0.1 to 15 Gyr) and metallicity ($[Z/H]$ from -2.3 to $+0.67$), as well as including a detailed modelling of the effects on indices of varying ‘ α ’-abundance ratios. However, fits were also obtained to the other model sets for comparison.

The process by which the best fits were obtained was iterative. First, fits were obtained for all galaxies using *all* the available indices. The pattern of deviations from the fit so obtained was then used to identify indices that matched the models poorly (see Fig. 4). Due to the problem of emission-line filling of the $H\delta$, $H\gamma$ and $H\beta$ Balmer lines in emission galaxies, we considered ‘passive’ and ‘emission’ galaxies (Section 3.1) separately. In Fig. 4 emission galaxies show the expected large deviation between observed and best fit model values of Balmer indices and Fe5015 (which is also emission-line affected). These indices were therefore omitted from the fitting procedure in emission galaxies.

Perhaps surprisingly, $H\beta$ and Fe5015 also deviate significantly in the ‘passive’ galaxies. We take this to indicate that, despite the rather severe definition of emission galaxies outlined in Section 3.1, at least some of the passive galaxies contain low-level emission that has escaped detection during our emission line measurements. Indeed, this was the main motivation for the stringent definition of emission-galaxies.

To minimise the effects of this low-level emission on our age and metallicity estimates, age sensitive $H\beta$ and metallicity sensitive Fe5015 indices were also excluded from the fits to passive galaxy data.

In both passive and emission galaxies Ca4455 was found to fall below best-fit model values. This effect has been noted in previous studies (e.g. Proctor & Sansom 2002; Clemens et al 2006). The flux-calibration sensitive Mg_1 and Mg_2 indices were also found to deviate from best fit model values. This was an anticipated effect, as 6dFGS spectra are only approximately flux calibrated and Mg_1 and Mg_2 have widely space pseudo-continuum bands. Ca4455, Mg_1 and Mg_2 were therefore excluded from the fitting procedure. Fortunately, most of the information lost by the exclusion of the Mg_1 and Mg_2 indices is captured in the Mgb index that is not sensitive to flux-calibration issues.

Once poorly fitting indices had been identified and

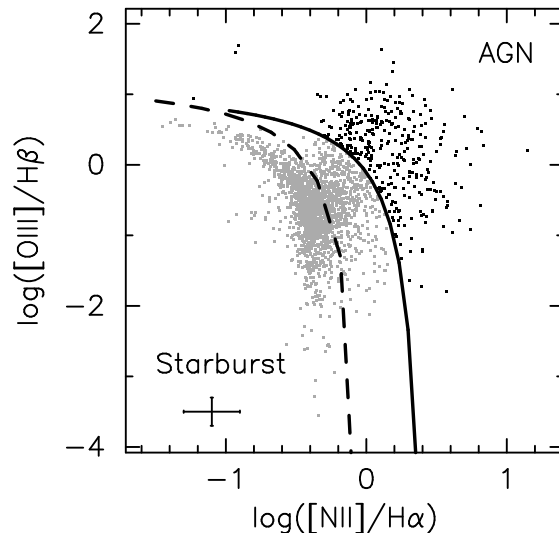


Figure 5. The $[OIII]/H\beta$ vs $[NII]/H\alpha$ emission line diagnostic diagram. NII , $H\alpha$ and $[OIII]$ were measured directly (see Section 3.1). $H\beta$ emission was estimated as the difference between observed and best-fit SSP model values of the $H\beta$ index (see Section 3.6). The average errors in the line-ratios are shown in the bottom-left of the plot. The solid line is from Kewley et al. (2001) and represents the theoretical dividing line between star-burst galaxies (grey points) and AGN (black points). The dashed line is the equivalent line from Kauffmann (2003a). Conservatively, we use the Kewley line to identify AGN.

omitted, the fitting of the remaining indices was carried out using a clipping procedure in which indices deviating from the model fit by more than 3σ were excluded, and the fitting procedure performed again. This results in an average of less than one additional index per galaxy being clipped from the fits. Most of the clipped indices could be associated with contamination from features such as the 5577 \AA sky-line. The resultant fits are based on between 10 and 15 indices and show good agreement between observed and best-fit values (Fig. 4). Indeed, the reduced- χ^2 values given in Fig. 4 (χ_r^2) were 1.08 and 1.30 for passive- and emission-galaxies respectively. This clearly indicates that our data are well represented by the models and that our errors reflect well the differences between observations and models.

3.7 Errors in derived parameters

For each galaxy in the sample, errors in $\log(\text{age})$ and $[Z/H]$ were estimated using 50 Monte-Carlo realisations of the best-fit model indices, assuming the observational errors for the galaxy in question. We again note that the reduced- χ^2 values of both passive- and emission-galaxies were close to one, indicating that the assumed errors reflect the average differences between observations and models quite well. The RMS scatter in the $\log(\text{age})$ and $[Z/H]$ values of the 50 realisations was therefore taken as the individual galaxy error. However, in an effort to better understand the detailed behaviour of the errors, deviations from the best-fit $\log(\text{age})$ and $[Z/H]$ values of all 50 realisations of each galaxy were retained and are presented in Section 4.3. For the purposes of the following analysis it is important that the derived ages are well defined. Therefore, ~ 1000 low signal-to-noise galax-

ies whose error in $\log(\text{age})$ exceeded 0.3 dex were deemed unreliable and were excluded from the analysis. The average errors for the remaining galaxies were ~ 0.15 dex in both $\log(\text{age})$ and $[Z/H]$.

4 RESULTS

4.1 Emission line galaxies

Emission lines can be used to separate star-burst and active galactic nuclei (AGN) galaxies using the $[\text{OIII}]\lambda 5007/\text{H}\beta$ – $[\text{NII}]/\text{H}\alpha$ diagnostic. Values of the $[\text{OIII}]\lambda 5007$, $[\text{NII}]$ and $\text{H}\alpha$ emission strengths were estimated from the 6dFGS spectra in a traditional manner (Section 3.1). The strength of $\text{H}\beta$ emission, however, was taken to be the deviation between the measured value of the $\text{H}\beta$ index and the best-fit SSP model value. Due to the relatively small observed dynamical range of $\text{H}\beta$ in absorption compared to that observed in emission, this is a fairly robust estimate of $\text{H}\beta$ emission. This is evidenced by the classic ‘Y’-shape evident in the diagnostic plot of $[\text{OIII}]\lambda 5007/\text{H}\beta$ against $[\text{NII}]/\text{H}\alpha$ shown in in Fig. 5. The position of the line dividing star-burst galaxies from AGN varies between studies in the literature. In Fig. 5 we show the lines given by Kewley et al. (2001) (solid line) and Kauffmann (2003a) (dashed line). In order to ensure reliable identifications of AGN we use the definition of Kewley et al. in the following. About 2200 of the 2700 emission galaxies in our sample have reliable estimates of all four of these emission lines, 300 of these lying in the region of the diagram associated with AGN as defined by Kewley et al. (2001).

4.2 Age and metallicity

In this section we outline the results of our age and metallicity determinations using Lick indices.

The distribution of ages and metallicities are presented in Fig. 6. The sample has been sub-divided into passive and emission-galaxies as described in Section 3.1. Emission-galaxies classified as AGN (Section 4.1) are shown as grey symbols, the remainder are plotted in black.

Before interpreting this plot, we must note the apparent clusterings and ‘zones-of-avoidance’, the clearest examples of which are evident in the emission galaxy plot. These are the inevitable result of linear interpolations in non-rectilinear spaces.

Returning attention to the actual results of our age and metallicity determinations; similar trends of increasing $[Z/H]$ with decreasing $\log(\text{age})$ are evident in both of passive and emission galaxies – albeit with emission galaxies tending to younger ages. Galaxies classified as possessing AGN in Section 4.1 also often possess young central ages.

We investigate the effect of aperture size on derived parameter using Fig. 7. In these plots, the galaxies with the largest and smallest sizes ($R_{K20} > 37.5$ arcsec and $R_{K20} < 7.5$ arcsec) are shown as red and blue points respectively. The blue points therefore represent the galaxies in which the 6.7 arcsec AAOmega aperture encompasses the largest fraction of galaxy light (on average $\sim 3.0 R_{eff}$), while the red points represent galaxies in which the smallest fraction of galaxy

light ($\sim 0.5 R_{eff}$) is encompassed by the fibre. The observed age–metallicity and age–velocity dispersion relations can be seen to be similar in these two extremes, with the most noticeable difference a slightly higher $[Z/H]$ (by ~ 0.1 dex) in large galaxies. We therefore find aperture-size effects to be generally small.

Due to the large, circular aperture of the 6dFGS, a direct comparison with the literature, which are mainly based on long-slit observations of galaxy centres, is not straight forward. Nevertheless, we note that the observed trend is at least qualitatively in agreement with the trends observed in previous studies (Trager et al. 2000; Proctor & Sansom 2002; Mehlert et al. 2003; Gallazzi et al. 2005; Colobert et al. 2006). The young central ages of AGN are also consistent with studies in the literature showing that star-bursts are often found to accompany AGN activity (e.g. see Cid Fernandes et al. 2004 and references therein).

An intriguing feature of Fig. 6 is the presence of a few old galaxies with extremely low $[Z/H]$ values, ($\lesssim -0.5$ dex). These galaxies, present in both passive and emission samples, possess a range of velocity dispersions. Visual inspection of both spectra and photometry generally reveals nothing exceptional about these galaxies. Further analysis of these galaxies are beyond the scope of this paper, but we note that their low numbers result in them having no impact on the results and conclusions of the present paper.

As in these literature studies, the slope in the age–metallicity relation exhibited by our data is similar to the slope of the age–metallicity degeneracy (Worthey 1994; ‘the 3/2 rule’). Before comparing these results with the photometry, it is therefore clearly important to establish that the age–metallicity degeneracy has been broken. To this end, in the following section we consider the errors in the derived parameters.

4.3 Errors in age and metallicity

As described in Section 3.7, errors in age and metallicity were characterised by considering the results of the 50 Monte-Carlo realisations of each of the 7000 galaxies in our sample. Fits using both the index combinations shown in Fig. 4 (with and without Balmer lines) were carried out for the purposes of this analysis (a total of approximately one million realisations). The differences between the input-model values of $\log(\text{age})$ and $[Z/H]$ and those of each of the realisations were calculated. These were combined in a number of bins depending upon the age–metallicity of the input models.

The analysis was also carried out using the *observed* index values as the inputs to the Monte-Carlo realisations (rather than the best-fit model values). No significant quantitative or qualitative differences were found.

Fig. 8 shows the results of this analysis as 1-sigma confidence contours for three age–metallicity bins. Each contour in these plots is based on tens of thousands of individual realisations of the best-fit galaxy data. The contour levels were defined as the iso-densities corresponding to e^{-1} of the peak values (as expected for the 1-sigma contour of a two-dimensional Gaussian distribution). The use of the iso-density peak in estimating the extent of 1-sigma confidence contours results in a small uncertainty in the esti-

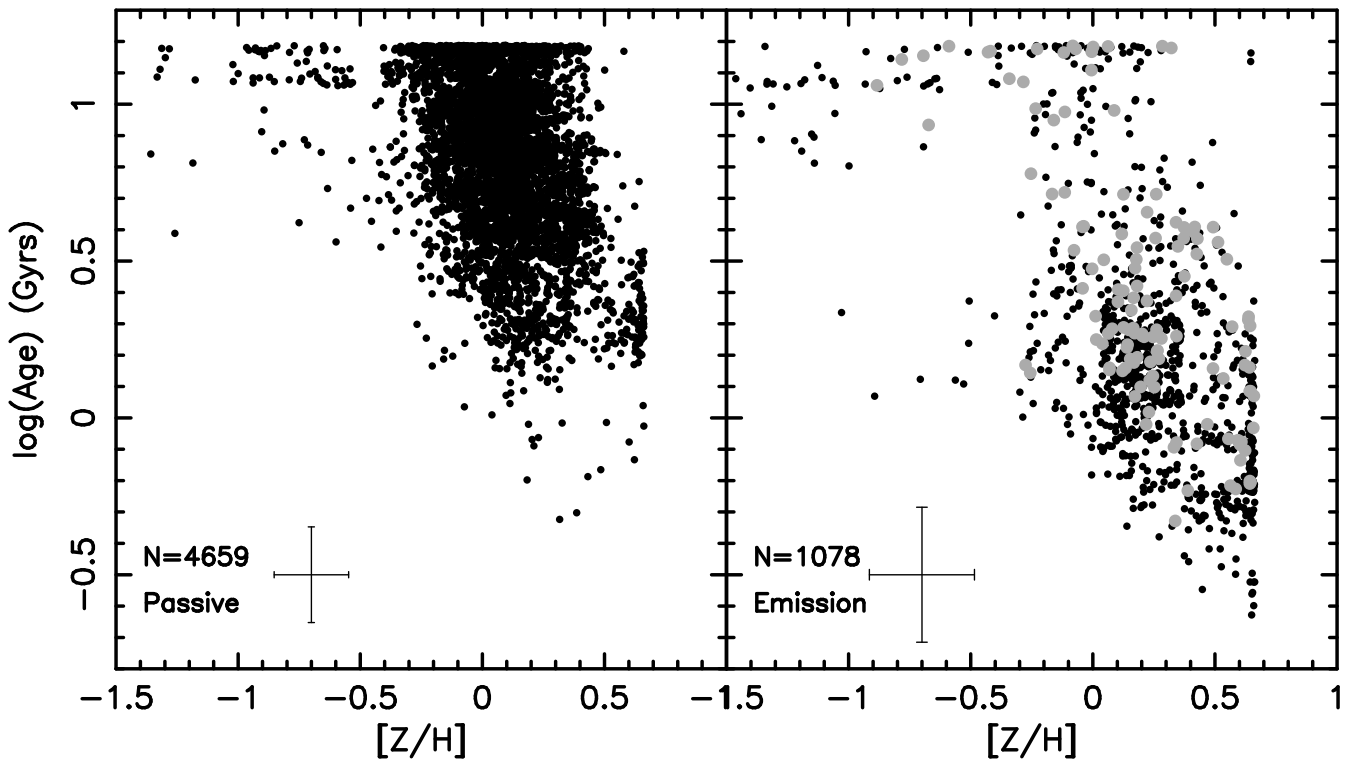


Figure 6. The ages and metallicities derived from the 6dFGS spectra separated by emission type (see Section 3.1). Grey points in the right-hand panel represent the AGN identified in Fig. 5. Average errors are shown in each plot. The overall loci of the points show that passive and emission galaxies largely follow similar trends between age and metallicity – albeit with emission galaxies tending to significantly younger ages.

mates. However, we estimate these to be of order 2% and therefore insignificant.

Results of the error analysis for both passive galaxies (in which Balmer indices were included in fits) and emission galaxies (in which Balmer indices were *excluded* from fits) are shown separately. We recall that $H\beta$ was excluded from all the fits. Fig. 8 also shows the data divided into two signal-to-noise ratio regimes ($S/N < 16 \text{ \AA}^{-1}$ and $S/N > 16 \text{ \AA}^{-1}$). Marginal distributions in $\log(\text{age})$ and $[Z/H]$ are shown at the edges of each main plot. We note that the positions of the contours in Fig. 8 were chosen for clarity only. To get a full picture one must imagine the whole surface of the $\log(\text{age})$ – $[Z/H]$ plane populated by such contours.

Fig. 8 shows that, as might be expected, error estimates increase with decreasing signal-to-noise-ratio. For passive galaxies, the analysis reveals $\log(\text{age})$ and $[Z/H]$ errors of ~ 0.1 dex in galaxies with S/N above ~ 16 . This falls to ~ 0.2 dex in galaxies with S/N below ~ 16 . The errors of the emission-galaxies (in which all Balmer lines are excluded from the fits) are somewhat larger, but are generally still of order 0.2 dex. It is therefore clear that while the age–metallicity degeneracy is still present (as evidenced by the sloped elliptical error contours in Fig. 8), the magnitude of the errors is sufficiently small for its effects to be negligible in our results – even in galaxies fit without Balmer lines. This is the result, and main advantage, of using large numbers (> 10) indices in the determination of ages and metallicities. The good age resolution achieved is emphasised in the marginal distributions of Fig. 8, in which galaxies older than 10 Gyr (1.0 dex), and galaxies younger than 1.5 Gyr

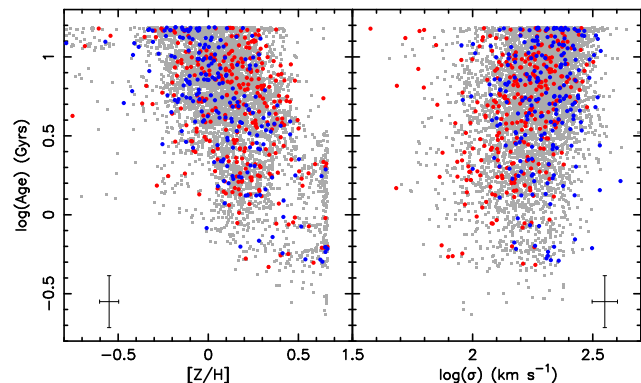


Figure 7. Age–metallicity and age– $\log(\sigma)$ are shown with colour representing galaxy (apparent) size. Blue points represent the smallest 5% of our sample, red points the largest 5%. Age–metallicity and age– $\log(\sigma)$ are shown to be largely independent of galaxy size.

(0.15 dex) (delimited by dashed lines in the marginal distributions) are largely uncontaminated by galaxies with ages of 3 Gyr (0.5 dex). Since the following analysis concentrates mainly on the very oldest and very youngest galaxies, these provide confidence that results do not suffer significantly from the effects of the age–metallicity degeneracy.

The final sample for which velocity dispersions and reliable age/metallicity estimates were measured consists of 4500 passive galaxies and 1000 emission galaxies.

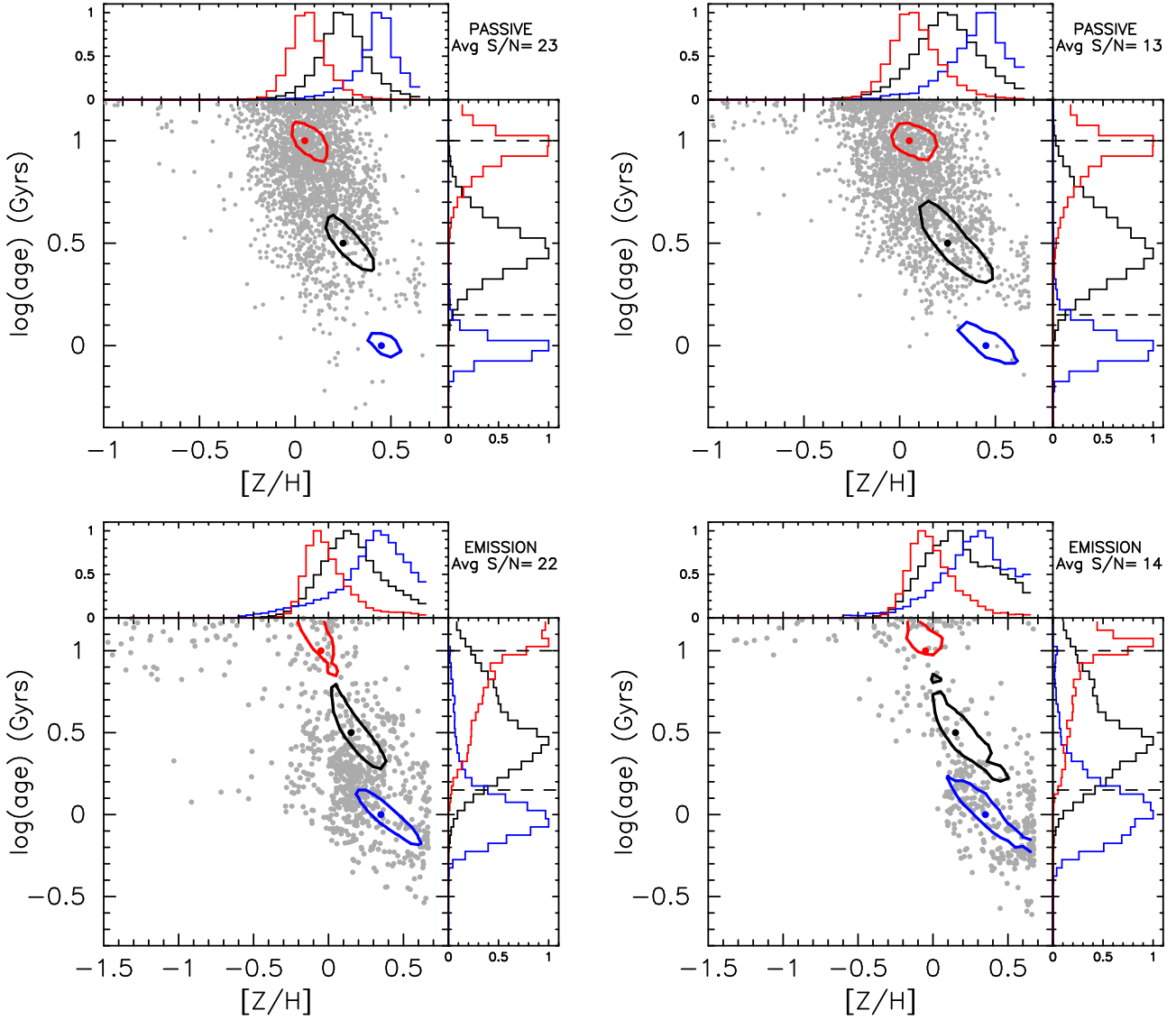


Figure 8. Error contours derived from the Monte-Carlo realisations of our galaxy sample are shown in three age–metallicity bins. Two signal-to-noise ratio subsamples are shown; $S/N > 16 \text{ \AA}^{-1}$ (left) S/N and $< 16 \text{ \AA}^{-1}$ (right). Results are given for both passive- (top) and emission-line (bottom) galaxies using the appropriate index combinations (see Section 3.6 and Fig. 4). The data for galaxies of appropriate emission characteristics and signal-to-noise-ratio are shown as grey points in each plot. Dashed lines in marginal distributions represent the upper and lower limits used to define the ‘young’ and ‘old’ samples respectively. Although the age–metallicity degeneracy is still present, its effects are minimised by the relatively small errors.

4.4 Photometric properties and dynamical masses

The combination of 6dFGS, 2MASS and SuperCOSMOS data permits the comparison for spectroscopic age and metallicity determinations to the B, R and K band photometric data for some 6000 galaxies. Specifically, by combining the photometry with the velocity dispersion measures from 6dFGS spectroscopy, we are able to investigate trends with age and metallicity in B, R and K band mass-to-light-ratios.

This analysis is carried out using a *dynamical* mass (M_{dyn}) calculated as:

$$M_{\text{dyn}} = \frac{C\sigma^2 R_{\text{eff}}}{G} \quad (3)$$

Where σ is the central velocity dispersion, R_{eff} is the half-

light radius and the constant C has a value of 5.0 (Cappellari et al. 2006). Unfortunately half-light radii are only available for 25% of our sample, while K band 20th magnitude isophotal radii (R_{K20}) are available for the entire sample. A calibration was therefore carried out by using Equation 3 to calculate masses for the galaxies in the 25% sub-sample (which also possess much more accurate, aperture corrected, velocity dispersion estimates), and comparing them with mass estimates using R_{K20} (instead of R_{eff}) in the same equation. A plot of the comparison is shown in Fig. 9. The correlation has equation $M_{\text{dyn}} = 1.068 M_{R_{K20}} - 1.223$ with only 0.12 dex of scatter. Given error estimates in M_{dyn} and $M_{R_{K20}}$ of 0.06 and 0.10 dex respectively, the correlation is clearly extremely good. Masses quoted throughout the remainder of this work are therefore those based on R_{K20} corrected as detailed.

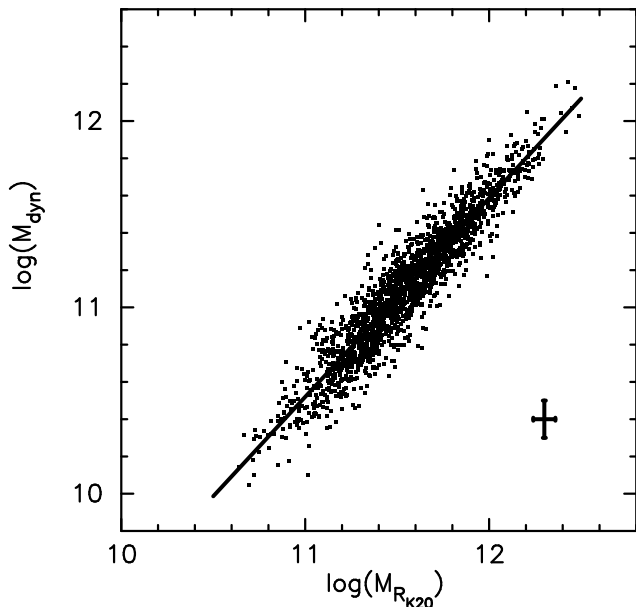


Figure 9. A comparison of dynamical mass (M_{dyn} ; Equation 3) with $M_{R_{K20}}$ (the mass estimate using R_{K20} in place of R_{eff}). The solid line shows the relation $M_{dyn}=1.068M_{RK20}-1.223$. The rms scatter about this line is 0.12 dex.

Age (Gyrs)	log(age) (dex)	[Z/H] (dex)	B (mag)	R (mag)	K (mag)
1	0.000	-0.4	5.27	4.40	2.67
3	0.477		6.61	5.33	3.24
11.7	1.105		7.92	6.46	4.15
1	0.000	0.0	5.53	4.52	2.61
3	0.477		6.94	5.55	3.20
11.7	1.105		8.32	6.73	4.15
1	0.000	0.4	5.91	4.72	2.27
3	0.477		7.29	5.76	3.03
11.7	1.105		8.79	7.01	4.04

Table 1. Examples of B, R and K magnitudes from BC03 for single stellar population models of varying age and metallicity are presented. Note that these values are used almost exclusively in a differential manner (see Section 4.4).

As well as the photometry of 2MASS and SuperCOSMOS, we also use the photometric results from the SSP models of Bruzual & Charlot (2003). Some key values from the Bruzual & Charlot models are shown in Table 1. We use these models almost exclusively to estimate differential properties; e.g. the rate of change of mass-to-light-ratio with $\log(\text{age})$ in populations of given $[Z/H]$. It should be noted that the rates of change of the photometric properties are reasonably constant with metallicity and age, as long as age is expressed in logarithmic form. This clearly indicates that a differential approach is a robust use of the model values. We shall flag the one occasion in which the models are used in a non-differential manner.

4.5 The effects of age and metallicity on photometric properties

This section details how the ages and metallicities derived from 6dFGS spectra for the central regions of galaxies are related to their *global* photometry. The analysis considers mainly the youngest (age < 1.5 Gyr) and oldest (age > 10 Gyr) galaxies. By concentrating on the two extremes in age we minimise the effects of the age–burst–strength degeneracy on our age and metallicity estimates. However, it is also important to note that the selection of galaxies with extremely young central populations has the effect of biasing the sample towards the *largest* bursts of star formation.

The following analysis utilises average values of galaxy parameters binned according to either mass or luminosity. The derived values are shown in Table 2. All colours and mass-to-light-ratios for the binned data were calculated from values in this table. We assume $M_{B,\odot}=5.47$, $M_{R,\odot}=4.28$ and $M_{K,\odot}=3.33$.

A mass-metallicity plot of the two sub-samples of our data is shown in Fig. 10¹. In this plot, galaxies younger than 1.5 Gyr are shown as black symbols; these galaxies possess an average $\log(\text{age})$ of 0.0 dex (1 Gyr). Galaxies older than 10 Gyr are shown as grey symbols; these possess an average $\log(\text{age})$ of 1.105 dex (12.7 Gyr). Results of the mass binning of metallicity values are shown in Fig. 10 as blue and red lines respectively. It is evident that the mass–metallicity relation detected varies with age. The logarithmic slope of the relation in old galaxies is ~ 0.25 , while the young galaxies are more metal rich than the old, and the data are consistent with no slope. An important aspect of our analysis will therefore be a consideration of the effects of these trends on mass-to-light-ratios. We also investigate implications for optical/near infrared colour-magnitude relations.

4.6 Mass-to-light-ratios in old galaxies

We consider first the ~ 1500 galaxies identified by our spectral analysis to possess ages older than 10 Gyr. Plots of $[M/L]$ against dynamical mass and K band luminosity for these galaxies are shown in Fig. 11. In each plot, the average values of the data in five bins along the x-axis (Table 2) are shown as solid lines. The extent of the rms scatter in each bin is identified by the dashed lines.

The observed trends between mass and mass-to-light-ratio in old galaxies vary with both waveband and variable against which they are plotted. In the K band, we find no trend in mass-to-light-ratio with luminosity, i.e. a slope consistent with zero. The other five plots all show trends with varying, non-zero slope. The logarithmic slopes in mass-to-light-ratio with mass are 0.231, 0.214 and 0.157 in B, R and K bands respectively, while the logarithmic slopes with luminosity are 0.093, 0.080 and 0.022 respectively. The typical formal errors on these logarithmic slopes are ~ 0.01 . These results are in good agreement with Trujillo, Burkert & Bell

¹ No significant difference was found between emission-types in these, and subsequent, figures. We therefore make no distinction between them, although we note that the majority of young galaxies are also emission galaxies, while, conversely, the majority of old galaxies are passive galaxies (Fig. 8).

Old, Mass binned						Old, Luminosity binned					
log(Mass)	[Z/H]	log(age)	M_B	M_R	M_K	log(Mass)	[Z/H]	log(age)	M_B	M_R	M_K
11.666	0.120	1.110	-20.993	-22.162	-25.497	11.755	0.137	1.107	-21.311	-22.507	-25.870
11.344	0.020	1.104	-20.372	-21.506	-24.769	11.411	0.038	1.101	-20.564	-21.715	-24.983
11.061	-0.040	1.109	-19.796	-20.908	-24.153	11.048	-0.032	1.107	-19.741	-20.866	-24.084
10.778	-0.136	1.105	-19.308	-20.395	-23.530	10.735	-0.138	1.107	-19.027	-20.112	-23.297
10.323	-0.276	1.101	-18.529	-19.546	-22.623	10.330	-0.213	1.104	-18.232	-19.222	-22.340
Young, Mass binned						Young, Luminosity binned					
log(Mass)	[Z/H]	log(age)	M_B	M_R	M_K	log(Mass)	[Z/H]	log(age)	M_B	M_R	M_K
11.648	0.363	0.062	-21.191	-22.216	-25.557	11.430	0.317	0.042	-21.366	-22.382	-25.728
11.331	0.421	-0.033	-20.745	-21.733	-24.959	11.209	0.311	-0.017	-20.781	-21.711	-24.948
11.062	0.394	-0.054	-20.432	-21.317	-24.569	10.870	0.276	0.023	-19.956	-20.878	-24.079
10.781	0.381	-0.011	-19.804	-20.694	-23.897	10.563	0.285	-0.025	-19.204	-20.015	-23.259
10.353	0.320	-0.025	-19.285	-20.130	-23.229	10.170	0.159	0.028	-18.545	-19.303	-22.332

Table 2. Binned average values of mass, metallicity, age and luminosity of old (>10 Gyr) galaxies (top) and young (<1.5 Gyr) galaxies (bottom). Binning was carried out in both mass (left) and K band luminosity (right).

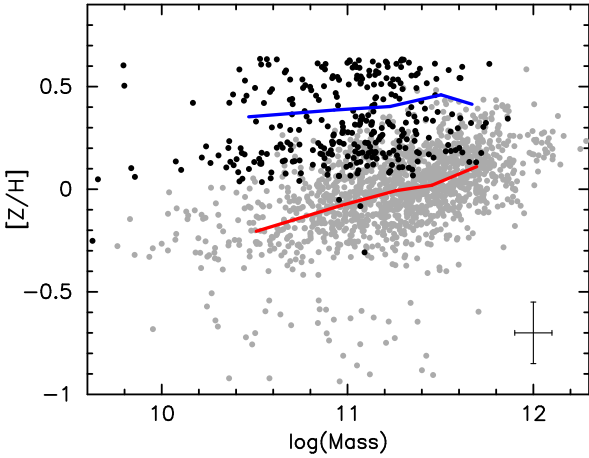


Figure 10. The relations between metallicity ($[Z/H]$) and mass is shown for young (<1.5 Gyr; black symbols) and old (>10 Gyr; grey symbols) galaxies. Mass-binned average values from Table 2) are shown for both old galaxies (red solid line) and young galaxies (blue solid line). While old galaxies exhibit a clear mass–metallicity relation, young galaxies do not.

(2004) who use a combined SDSS/2MASS catalogue to investigate mass-to-light-ratios in the B and K bands (but without the luxury of spectroscopy). They found similar slopes in B and K band stellar mass-to-light-ratios with luminosity of 0.07 and 0.02 dex respectively.

While the effects of age are almost entirely eliminated by our consideration of only old galaxies, the effects of metallicity have yet to be accounted for. The effects of the mass–metallicity relation shown in Fig. 10 on mass-to-light-ratios are investigated in Fig. 12. This figure again shows the binned data from Fig. 11 as thick solid lines. Also shown are the values after correction of the mass-to-light-ratio for differences in metallicity (dashed lines). The corrections are made by comparing the luminosities predicted by BC03 models for SSPs of the metallicity (and age) of each mass or luminosity bin (Table 2) with the corresponding prediction for the highest mass/luminosity bin (Table 2). The dashed lines in the left hand plots therefore represent the observed trends between dynamical mass and mass-to-

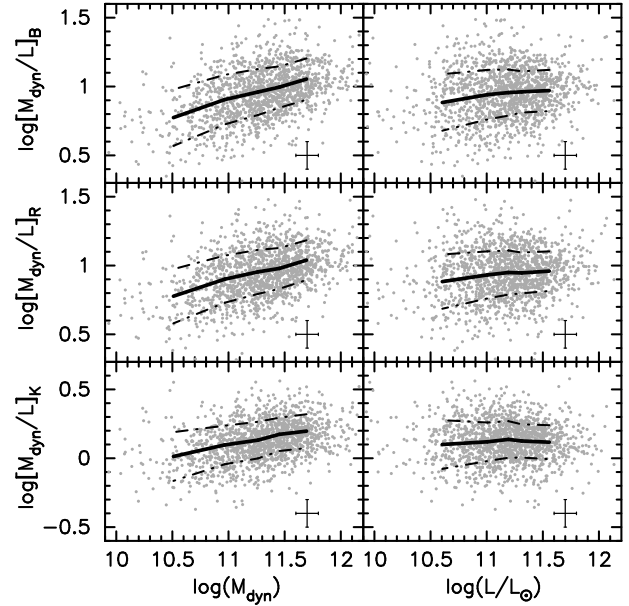


Figure 11. The dynamical mass-to-light-ratios of old galaxies in B, R and K bands are plotted against dynamical mass and K band luminosity. Solid lines represent averages in five bins along the x-axis. The extent of the rms scatter is identified by dashed lines. The average error on individual points shown in the bottom right of each plot.

light-ratio in old galaxies (solid lines) after correction for the mass–metallicity relation evident in Fig. 10 and Table 2. Similarly, the dashed lines in the right hand plots represent the observed trends between luminosity and mass-to-light-ratios (solid lines) after correction for the luminosity–metallicity relation evident Table 2. The dashed lines can therefore be considered the relations for old galaxies of fixed metallicity. We note that the K band relations are almost unaffected by the corrections. This is due to the lack of sensitivity of K band luminosity to metallicity (see Table 1).

The agreement between corrected $\log[M/L]$ values is extremely good, with logarithmic slope against mass of ~ 0.15 in all three bands. Against luminosity we find logarithmic slopes in the corrected values of -0.014 , 0.010 and 0.031 in

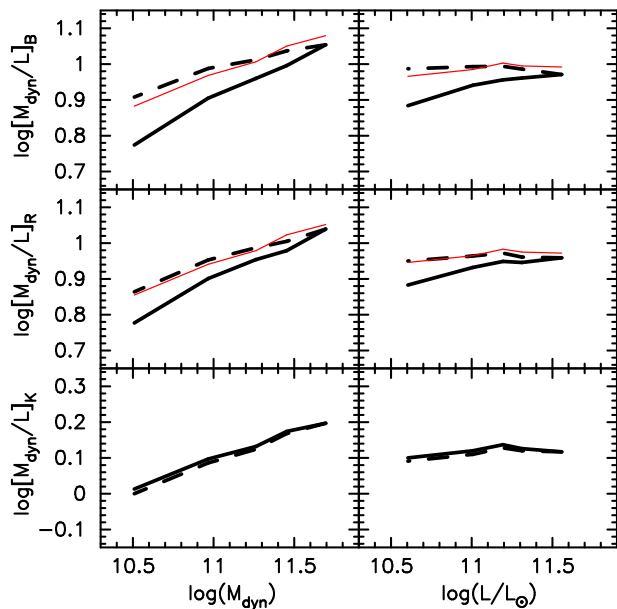


Figure 12. Plot of mass-to-light-ratio in B, R and K bands against dynamical mass and K band luminosity. Thick solid lines reproduce the binned averages of the old galaxies from Fig. 11. Thick dashed lines represent these values corrected for metallicity. In B and R band plots, the K band profile is reproduced (after and offset ~ 0.9 dex) as a thin red line. The metallicity corrected values are remarkably consistent across the three wavebands.

B, R and K bands respectively. With formal errors of ~ 0.01 these are broadly consistent with a slope of zero. The remarkable consistency between the results for the three individual wavebands suggest that the ages, metallicities and photometric predictions of the BC03 models are both reliable and internally consistent, at least when they are used in the differential sense employed in this work.

The results are also again in good agreement with Trujillo, Burkert & Bell (2004), who find slopes equivalent to 0.20 and 0.14 in B and K bands respectively (compared to our 0.23 and 0.15). With the benefit of spectroscopy, we are able to clearly identify metallicity as the main contributor to the stellar population effects. Our results are also in good general agreement with the previous studies of both Bernardi et al. (2003b) and Padmanabhan et al. (2004), who find similar trends in dynamical mass-to-light-ratios for large numbers of SDSS galaxies.

4.7 The fundamental plane

While our data are not suitable for a direct analysis of the Fundamental Plane it is nonetheless interesting to compare our results with such studies in the literature. To this end we examined the implications of the varying slopes in mass-to-light-ratio with mass with waveband on fits to the Fundamental Plane (FP). The implications can be investigated using the *measured* slopes in $\log[M/L]$ with mass for old galaxies (Table 2 and Figs 11 and 12). Using these values it is possible to predict the FP (given by $\log(R) = \alpha \log(\sigma) + \beta \log \langle I \rangle + \gamma$) that one would expect to find using;

$$\alpha = \frac{2(1-s)}{1+s}, \quad (4)$$

and

$$\beta = \frac{-1}{1+s}. \quad (5)$$

Where $\langle I \rangle$ is the average surface brightness within the effective radius (R) and s is the observed slope in $\log[M/L]$ with $\log(\text{Mass})$ from Table 2. The virial theorem for homologous systems (i.e. in the absence of a tilt) would predict $\alpha = 2$ and $\beta = 1$.

The results of the comparisons between predicted α and β and the (observational) literature values are shown in Table 3. The predictions using the observed slopes in mass-to-light-ratio with mass compare very well to the literature, values (consistent with the predictions to within $\sim 2\sigma$). We note that this is despite both our indirect approach as well as literature studies not having the luxury of isolating old galaxies.

The comparisons indicate that, while most of the tilt of the FP is dynamical in origin, the mass-metallicity relation in galaxies (Fig. 10) causes an increasing α and β with wavelength² due to the *decreasing* sensitivity to metallicity of photometry at increasing wavelength. This trend culminates in the observed FP tilt in the K band being almost identical to the underlying dynamical tilt in the FP (see previous section). This is again due to the lack of sensitivity of K band luminosity to metallicity in old stellar populations, which makes the K band an excellent tool for probing mass-to-light-ratios in old (or uniform age) stellar populations.

We have therefore shown our results to be consistent with a broad range of previous studies of galaxy mass-to-light-ratios and the Fundamental Plane. However, the conclusions we draw are not. To understand why this is the case, recall that the observed ‘tilt’ in the Fundamental Plane is often interpreted as a trend in mass-to-light-ratio with mass or luminosity. Indeed, a trend with mass of the form $[M/L] \propto M^s$ was the starting point of the previous consideration of the Fundamental Plane. However, careful consideration of the data show there is a flaw in this interpretation. The relation $[M/L] \propto M^a$ can be simply rearranged into the form $[M/L] \propto L^b$. This gives $b = \frac{a}{1-a}$. Therefore, for $a=0.15$, we would expect $b=0.18$, in stark contrast with the $b=0$ found. We must therefore conclude that the simple picture of a trend in dynamical mass-to-light-ratios with either mass or luminosity is excluded by our data.

In summary, we have shown that our observations are generally in good agreement with previous literature studies. Furthermore, we have shown that the mass-metallicity relation with logarithmic slope 0.25 found in the data is sufficient to explain the differences in the observed trends in mass-to-light-ratios with mass and luminosity in B, R and K bands as well as the variations in the apparent ‘tilt’ found in previous studies of the Fundamental Plane. However, once this stellar population effect has been removed, a significant (and consistent) trend in mass-to-light-ratio with

² Similar trends in α and β with wavelength were found by Bernardi et al. (2004) for the galaxy colours in the SDSS.

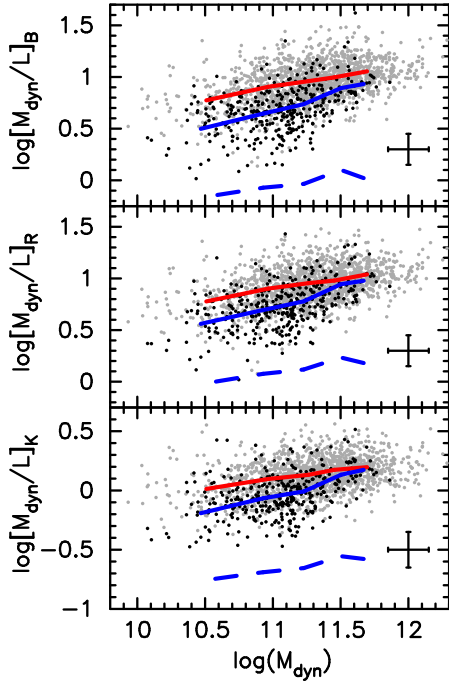


Figure 13. Mass-to-light-ratio in B, R and K bands against mass for both young and old galaxies. Average errors on data points are shown in each plot. Mass-binned averages of old and young galaxies are shown as red and blue lines respectively. Blue dashed lines represent the mass-to-light-ratios *expected* in the young galaxies based on their central spectroscopic ages and metallicities. While young galaxies deviate from the old population in a sense consistent with their younger ages, none have mass-to-light-ratios as low as their central ages would imply.

mass remains in all three wavebands. Finally, we find that the data *rules out* simple models of variations in dynamical mass-to-light-ratio with mass *or* luminosity. Further analysis will require a detailed consideration of the distribution of galaxies in the full 3-dimensional space of the Fundamental Plane. This is planned for a future paper. In this work we proceed by exploring the effects on photometry of young central spectroscopic ages.

4.8 The effects of age on mass-to-light-ratio

We now turn our attention to the effects of the young central populations detected in our 6dFGS spectra on the global properties of galaxies as indicated by their photometry. There are 400 ‘young’ (<1.5 Gyr) galaxies (see Section 4.5) included in this analysis.

Plots of mass-to-light-ratio with mass for both young and old galaxies are shown in Fig. 13. Mass-binned averages of young and old data are shown as blue and red solid lines respectively. Also shown in these plots as dashed blue lines are model predictions of the effects of the differing ages and metallicities of the young and old populations in each mass bin. These are based on the comparison of luminosity values from the BC03 SSP models for the differences in age and metallicity of the young and old galaxies in each mass bin. A direct comparison of the data for young galaxies to these lines would therefore implicitly assume that the young central populations detected in the spectroscopy pervade the

galaxies’ populations *as a whole* - i.e represents the same fraction of the galaxy population at all radii³.

Young galaxies can be seen to be displaced with respect to the old galaxies in a sense consistent with their young ages. However, the displacements are small compared to the predicted values. They also become smaller towards higher masses. The data therefore show that, on average: (i) young populations do *not* pervade their host galaxies, but are instead centrally concentrated; ii) young populations must constitute relatively small fractions of total galaxy masses; and (iii) the mass fraction in the form of a young stellar population must decrease with increasing galaxy mass.

To quantify these conclusions, for each mass bin, the fraction of total galaxy stellar mass and luminosity involved in the recent star-burst (f_M and f_L) were estimated. These estimates were made by a differential comparison of the BC03 predictions for mass-to-light-ratios to the observed values. In each waveband, the difference between the observed mass-to-light-ratios of the young galaxies from those of the old galaxies in the same mass bin ($\Delta \log[M/L]_{obs}$) was compared to the difference between model predictions for young and old populations of appropriate metallicity ($\Delta \log[M/L]_{model}$). Denoting these mass-to-light-ratio differences as s and r respectively, we derive:

$$f_M = \frac{10^{-\Delta \log[M/L]_{obs}} - 1}{10^{-\Delta \log[M/L]_{model}} - 1} \quad \text{or} \quad \frac{10^{-s} - 1}{10^{-r} - 1}. \quad (6)$$

The derivation of Equation 6 is given in Appendix A. We estimate the *luminosity* fraction in the recent burst by:

$$f_L = \frac{rf_M}{(1 - f_M) + rf_M}. \quad (7)$$

Finally, the total mass (M_{burst} , in solar masses) is estimated by:

$$M_{burst} = f_M \cdot M_{gal}. \quad (8)$$

Where M_{gal} is the total mass of the galaxy. The derivation of these expressions again assumes that the young populations at any given mass are seen against a background old population with a metallicity and mass-to-light-ratio appropriate to that mass (as given by the mass-binned values for old galaxies in Table 2). The young stellar population is nonetheless assumed to *dominate the central regions* (such that issues related to degeneracies with burst-strength do not arise).

The estimates of mass- and luminosity-fractions and burst-masses are plotted against galaxy mass in Fig. 14. Despite the (expected) variation in luminosity fractions between wavebands, agreement between the values for the mass fractions derived from the three wavebands is extremely good. This suggests that both our assumption of the same underlying dynamical ‘tilt’ in young galaxies as exhibited by old galaxies is correct, and that our age and metallicity corrections are accurate. The trend shows a decreasing mass fraction with increasing mass falling from $\sim 10\%$ at $10^{10.5} M_\odot$ to 2% at $10^{11.5} M_\odot$. This is in agreement with the study of Treu et al. (2005), who find the stellar fraction

³ The analysis also implicitly assumes that the dynamical trends observed in old galaxies, whatever their cause, are also present in the young galaxies.

Band	Predictions		Literature		References
	α	β	α	β	
B	1.25	-0.81	1.20 ± 0.06	-0.83 ± 0.02	Jørgensen et al. (1996) Dressler et al. (1987)
			1.33 ± 0.05	-0.83 ± 0.03	
R	1.29	-0.82	1.22 ± 0.09	-0.84 ± 0.03	Colless et al. (2001a)
			1.37 ± 0.04	-0.825 ± 0.01	Gibbons et al. (2001)
			1.38 ± 0.04	-0.82 ± 0.03	Hudson et al. (1997)
K	1.46	-0.86	1.53 ± 0.08	-0.79 ± 0.03	Pahre et al. (1998)

Table 3. Fundamental Plane coefficients. Values predicted from the slopes of mass-to-light with mass from Table 2 (see Section 4.6) are shown in the left-hand column. These are to be compared with the values from the literature and values derived in this work. Good agreement is found.

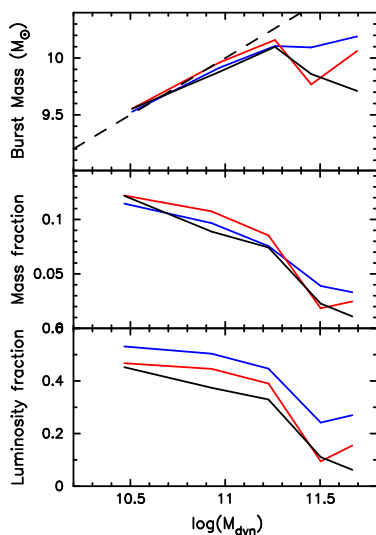


Figure 14. The average luminosity (bottom) and mass (middle) fractions in recent bursts are plotted against average galaxy mass for the five mass bins of Figure 11. Values derived from the B, R and K bands are shown in blue, red and black lines respectively. Also shown (top) are estimates of the actual masses (in M_{\odot}) involved in the recent bursts. A fixed 10% fraction is indicated by the dashed line. Agreement in mass estimates between wavebands is extremely good, suggesting an upper limit to the size of star bursts in these galaxies.

formed in recent times varies from 20%-40% below $10^{11} M_{\odot}$, to below 1% above $10^{11.5} M_{\odot}$.

Also shown in Fig. 14 are the estimates of average total mass involved in the recent burst of star formation. Agreement between wavebands is again good. However, the absolute values given here must be treated with caution, as they are calculated by the only non-differential application of BC03 models used in this work. Nevertheless, in a relative sense, the data exhibit a narrow range of burst-masses and an apparent *upper limit* on their size in high mass galaxies.

4.9 Colour-magnitude relations

As a final consideration we next investigate the implications of our findings for colour-magnitude relations. Note that these relations are independent of dynamical effects.

In Fig. 15 we plot the colour-magnitude relations B–K and R–K against M_K . Galaxies with both old (grey points)

and young (black points) central populations are shown. Averages (binned by luminosity) of the old and young populations are again shown as solid red and blue lines respectively. Slopes in the old galaxies are in good accord with literature values (thin black lines in each plot). As the sample includes late-type galaxies, particular amongst the young galaxies, these must lie close to the ‘red sequence’ in our colour-magnitude diagrams. This suggests they therefore correspond to the ‘dusty red-sequence’ of Wolf, Gray & Meisenheimer (2005). The lack of galaxies in the ‘blue-cloud’ is almost certainly the result of a number of selection effects. These include the effects of template mismatches during velocity dispersion measurements and the removal of galaxies with poor fits or large errors during age/metallicity measurement.

Fig. 15 shows that, for both colours, young galaxies tend to be bluer than the old galaxies. However, the offsets are extremely small. Our results from the previous section indicate that this is largely the result of the low mass fractions formed in the recent star formation events. Fig. 15 therefore shows that galaxies lying on, or close to, the red sequence may not be ‘red and dead’, but may still be forming modest numbers of new stars. Indeed, we note that *most* of the galaxies with young central populations also exhibit on-going star formation (Fig. 6).

5 CONCLUSIONS

We have measured ages and metallicities from the 6dFGS spectra of ~ 7000 galaxies of all morphological and emission types. We have demonstrated that the age–metallicity degeneracy has been broken in this study, particularly with regard to the very young and very old galaxies used in the subsequent analysis. These data for the *central regions* are compared with the *global* photometry from 2MASS and SuperCOSMOS for the ~ 6000 galaxies for which such photometry is available. Combining spectroscopy and photometry we are able to investigate trends in global B, R and K band mass-to-light-ratios with the central stellar populations of the galaxies.

An age–metallicity trend is identified in passive galaxies that is consistent with the results of similar studies in the literature. The stellar populations of galaxies exhibiting emission lines (arising from either star-bursts or AGN)

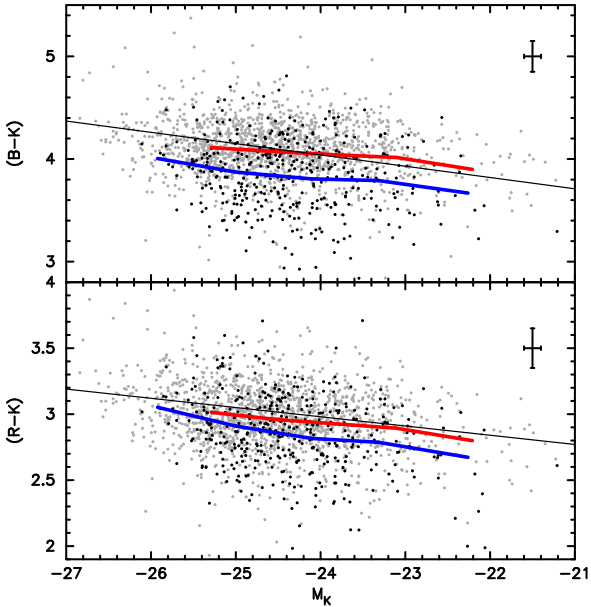


Figure 15. The colour-magnitude relations B–K and R–K against M_K are shown for both young and old galaxies. Luminosity-binned average values are shown as blue and red lines respectively. Young galaxies are, as expected, bluer than old.

follow a similar trend, but exhibit younger ages than their passive counterparts.

To minimise the effects of complex mixtures of stellar populations, we confine our analysis to the data for very old or very young galaxies. We find a steep mass-metallicity relation in old galaxies (logarithmic slope of ~ 0.25), while in young galaxies the trend is consistent with zero slope.

Using only the old galaxies, we find a dynamical trend in mass-to-light-ratios with mass of logarithmic slope ~ 0.15 . This is in good agreement with values reported in the literature. However, there is no agreement in the literature as to the cause of this tilt. Padmanabhan et al. (2004) concluded that most of the tilt is due to variations in dark matter content. From the modelling perspective, Robertson et al. (2006) perform simulations of a series of mergers and investigate the scaling relations of their merger remnants. From mergers of gas-rich disk galaxies they derive a FP with $\alpha = 1.55$ and $\beta = 0.82$, in good agreement with our K band values (see Table 3). In their models the tilt away from the virial scaling relation is caused by gas dissipative effects and not dark matter content. Trujillo et al. (2004) on the other hand attribute the tilt to ‘non-homology’, deriving almost identical contributions to the tilt from dynamical and stellar population effects as those we find in this work. Our findings, however, also show that whatever the cause of the tilt, it is not a simple in mass-to-light-ratio (or its scatter) with mass or luminosity. Instead we find that a more complex description will be required; this will be a subject of a future paper.

Considering extremely young galaxies, our results show that the properties of the central stellar populations identified by the spectroscopy do *not* generally correlate with the global properties of their host galaxies. Indeed, the data indicate that recent bursts of star formation are limited to a mass of $\lesssim 10^{10} M_\odot$ and are strongly centrally concentrated.

Consequently, in high mass galaxies exhibiting young central populations, recent star forming events have negligible effect on their global photometry. As a consequence we have shown that galaxies sitting on, or near, the red sequence may not be ‘red and dead’, but may still be forming modest numbers of new stars.

We therefore conclude that the young ages found in studies of galaxy centres in this and other spectroscopic studies should not be considered representative of the age of their host galaxies as a whole. They may, however, be reasonably interpreted as indicators of recent assembly events. As a result of these considerations, the small scatter in photometric scaling relations, which initially motivated the monolithic collapse models, ceases to be inconsistent with either the hierarchical merging model or the results of the Lick index studies indicating young central populations.

In future work we will include the results from the completed 6dF Galaxy Survey and report on the full chemical properties (including α -abundance ratios) of the central regions of galaxies. The effective radii, peculiar velocities and environmental parameters of the 6dFGS sample, currently being analysed by the 6dFGS team, will be included. This will allow not only more accurate determination of photometric properties and a more detailed analysis of the Fundamental Plane, but also the investigation of the strong *quantitative* predictions of trends in galaxy formation/assembly epochs and metals-content with galaxy mass and environment.

Acknowledgements

This publication makes use of data products from the Two Micron All Sky Survey (2MASS), which is a joint project of the University of Massachusetts and the Infrared Processing and Analysis Center/California Institute of Technology, funded by the National Aeronautics and Space Administration and the National Science Foundation.

The authors acknowledge the data analysis facilities provided by IRAF, which is distributed by the National Optical Astronomy Observatories and operated by AURA, Inc., under cooperative agreement with the National Science Foundation. We thank the Australian Research Council for funding that supported this work.

The measuring of line values from 6dFGS spectra was begun in Philip Lah’s Honours Thesis 2003 ‘Exploring the Stellar Population of Early-Type Galaxies in the 6dF Galaxy Survey’ which looked at the 6dFGS Early Data Release, (December 2002). This Honours thesis was supervised by Matthew Colless and Heath Jones. Assistance with the software used in this work was provided by Craig Harrison. Lachlan Campbell provided additional assistance with the 6dFGS data particularly with the velocity dispersions and 6dF arc spectra. The authors also thank Chris Blake for valuable input.

1 Appendix 1. Mass fraction derivation

The logarithm of the mass-to-light ratio in a galaxy comprising two populations; one young and one old, can be written:

$$\log[M/L]_{\text{obs}} = \log\left[\frac{M}{L_{\text{old}} + L_{\text{young}}}\right]. \quad (1)$$

This parameterisation assumes that the mass of the galaxy is unaffected by the starburst that generates the young stellar population (the galaxy converts some of its own mass into stars).

Now, expressing the fraction of the observed stellar mass in young stars as f_M and the ratio of mass-to-light-ratios of young and old populations as r , we can write:

$$\log[M/L]_{\text{obs}} = \log\left[\frac{M}{(1-f_M)L_{\text{old}} + rf_M L_{\text{old}}}\right]. \quad (2)$$

Rearranging:

$$\log[M/L]_{\text{obs}} = \log[M/L]_{\text{old}} - \log((1-f_M) + rf_M). \quad (3)$$

Defining:

$$\Delta \log[M/L]_{\text{obs}} = \log[M/L]_{\text{obs}} - \log[M/L]_{\text{old}}. \quad (4)$$

We get;

$$\Delta \log[M/L]_{\text{obs}} = -\log((r-1)f_M + 1). \quad (5)$$

Rearranging:

$$10^{-\Delta \log[M/L]_{\text{obs}}} = (r-1)f_M + 1, \quad (6)$$

and;

$$f_M = \frac{10^{-\Delta \log[M/L]_{\text{obs}}} - 1}{r - 1} \quad (7)$$

The ratio of mass-to-light-ratios (r), as defined above can be estimated using the BC03 models of appropriate age and metallicity:

$$r = 10^{\log[M/L]_{\text{BC03old}} - [\log[M/L]_{\text{BC03young}}]} \quad (8)$$

I.e:

$$r = 10^{-\Delta \log[M/L]_{\text{model}}} \quad (9)$$

We thus derive the fraction of the stellar mass in the 1 Gyr old population as:

$$f_M = \frac{10^{-\Delta \log[M/L]_{\text{obs}}} - 1}{10^{-\Delta \log[M/L]_{\text{model}}} - 1} \quad (10)$$

We note that, by the differential use of both the observations and models, mass fractions are derived *without* knowledge of the true stellar to dynamical mass ratios.

References

Baldry I.K. et al., 2002, ApJ, 569, 582
 Baum W.A., 1959, IAU Symp. 10, The Hertzsprung-Russell Diagram, ed. J. L. Greenstein (Paris: IAU), 23
 Bernardi M. et al., 2003a, AJ, 125, 1882
 Bernardi M. et al., 2003b, AJ, 125, 1866
 Bernardi M. et al., 2006, AJ, 131, 2018
 Bernardi M., 2007, AJ, 133, 1954
 Blumenthal G.R., Faber S.M., Primack J.R., Rees M.J., 1984, Nature, 311, 517
 Bower R.G., Lucy J.R., Ellis R.S., 1992a, MNRAS, 254, 589
 Bower R.G., Lucy J.R., Ellis R.S., 1992b, MNRAS, 254, 601
 Bruzual A.G., Charlot S., 2003, MNRAS, 344, 1000
 Caldwell N., Rose J.A., Concannon K.D., 2003, AJ, 125, 2891
 Cappellari M. et al., 2006, MNRAS, 366, 1126
 Carlberg R.G., 1984, ApJ, 286, 403

Chang R., Gallazzi A., Kauffmann G., Charlot S., Ivezić Ž., Brinchmann J., Heckman T.M., 2006, MNRAS, 366, 717
 Cid Fernandes R., Gu Q., Melnick J., Terlevich E., Terlevich R., Kunth D., Rodrigues Lacerda R., Joguet B., 2004, MNRAS, 355, 273
 Cid Fernandes R., Mateus, A., Sodr e L., Stasinska G., Gomes J.M., 2005, MNRAS, 358, 363
 Clemens M.S., Bressan A., Nikolic B., Alexander P., Annibali F., Rampazzo R., 2006, MNRAS, 370, 702
 Colless M., Saglia R.P., Burstein D., Davies R.L., McMahan Jr R.K., Wegner G., 2001a, MNRAS, 321, 277
 Colless M. et al., 2001b, MNRAS, 328, 1039
 Collobert M., Sarzi M., Davies R.L., Kuntschner H., Colless M., 2006, MNRAS, 370, 1213
 De Lucia G., Springel V., White S.D.M., Croton D., Kauffmann G., 2006, MNRAS, 366, 499
 Dressler A., Lynden-Ball D., Burstein D., Faber S.M., Terlevich R., Wegner G., 1987, ApJ, 313, 42
 Eisenstein D.J. et al., 2003, ApJ, 585, 694
 Fernandes R.C., Mateus, A., Sodr e L., Stasinska G., Gomes J.M., 2005, MNRAS, 358, 363
 Gallazzi A., Charlot S., Brinchmann J., White S.D.M., Tremonti C., 2005, MNRAS, 362, 41
 Gebhardt, K. et al., ApJ, 539, L13
 Gibbons R.A., Fruchter A.S., Bothun G.D., 2001, AJ, 121, 649
 Gonz alez J. J., 1993, PhD thesis, Univ. California
 Hambly N.C., Irwin M.J., MacGillivray H.T., 2001, MNRAS, 326, 1295
 Hudson M.J., Lucey J.R., Smith R.J., Steel J., 1997, MNRAS, 291, 488
 Jarrett T.H., Chester T., Cutri R., Schneider S., Skrutskie M., Huchra J.P., 2000a, AJ, 119, 2498
 Jarrett T.H., Chesse, T., Cutri R., Schneider S., Rosenberg J., Huchra J.P., Mader J., 2000b, AJ, 120, 298
 Jones D.H. et al., 2004, MNRAS, 355, 747
 Jones D.H., Peterson B.A., Colless M., Saunders W., 2006, MNRAS, 369, 25
 J rgensen I., Franx M., Kj ergaard P., 1995, MNRAS, 276, 1341
 J rgensen I., Franx M., Kj ergaard P., 1996, MNRAS, 280, 167
 Kauffmann G., 1996, MNRAS, 281, 487
 Kauffmann G. et al., 2003, MNRAS, 346, 1055
 Kauffmann G. et al., 2003a, MNRAS, 341, 33
 Kauffmann G. et al., 2003b, MNRAS, 341, 54
 Kewley L.J., Dopita M.A., Sutherland R.S., Heisler C.A., Trevena J., 2001, ApJ, 556, 121
 Korn A.J., Maraston C., Thomas D., 2005, A&A, 438, 685
 Larson R.B., 1974, MNRAS, 166, 585
 Lewis I. et al., 2002, MNRAS, 334, 673
 Mehlert D., Thomas D., Saglia R.P., Bender R., Wegner G., 2003, A&A, 407, 423
 Moore S.A.W., 2001, Ph.D thesis, Univ of Durham
 Padmanabhan N. et al., 2004, New Astron., 9, 329
 Pahre M.A., Djorgovski S.G., de Carvalho R.R., 1998, AJ, 116, 1591
 Proctor R.N., Sansom A.E., 2002, MNRAS, 333, 517
 Proctor R.N., Forbes D.A., Beasley M.A., 2004a, MNRAS, 355, 1327
 Proctor R.N., Forbes D.A., Hau G.K.T., Beasley M.A., De Silva G.M., Contreras R., Terlevich A.I., 2004b, MNRAS,

- 349, 1381
Proctor R.N., Forbes D.A., Forestell A., Gebhardt K., 2005, MNRAS, 362, 857
Robertson B., Cox T.J., Hernquist L., Franx M., Hopkins P.F., Martini P., Springel V., 2006, ApJ, 641, 21
Smith R.J., Hudson M.J., Lucey, J.R., Nelan, J.E., Wegner, G.A., 2006, MNRAS, 369, 1419
Spergel D.N. et al., 2003, ApJS, 148, 175
Terlevich A.I., Forbes D.A., 2002, MNRAS, 330, 547
Thomas D., Maraston C., Bender R., 2003, MNRAS, 339, 897
Thomas D., Maraston C., Bender R., Mendes de Oliveira C., 2005, ApJ, 621, 673
Thomas D., Maraston C., Korn A., 2004, MNRAS, 351, 19
Trager, S., Faber, S., Worthey, G., Gonzalez, J., 2000, AJ, 120, 165
Tremonti C. et al., ApJ, 613, 898
Treu T., Ellis R.S., Liao T.X., van Dokkum P.G., Tozzi P., Coli, A., Newman J., Cooper M.C., Davis M., 2005, ApJ, 633, 174
Trujillo I., Burkert A., Bell E.F., 2004, AJ, 600, L39
White S.D.M., Rees M.J., 1978, MNRAS, 183, 341
Wolf C., Gray M.E., Meisenheimer K., 2005, A&A, 443, 435
Worthey G., 1994, ApJS, 95,107
Worthey G., Ottaviani D.L., 1997, ApJS, 111, 377
York D.G. et al., 2000, AJ, 120, 1579